Observation of Moisture Tendencies Related to Shallow Convection

H. BELLENGER, K. YONEYAMA, AND M. KATSUMATA

Japan Agency for Marine-Earth Science and Technology, Yokosuka, Japan

T. NISHIZAWA

National Institute for Environmental Studies, Tsukuba, Japan

K. YASUNAGA

Department of Earth Science, University of Toyama, Toyama, and Japan Agency for Marine-Earth Science and Technology, Yokosuka, Japan

R. SHIROOKA

Japan Agency for Marine-Earth Science and Technology, Yokosuka, Japan

(Manuscript received 13 February 2014, in final form 23 October 2014)

ABSTRACT

Tropospheric moisture is a key factor controlling the global climate and its variability. For instance, moistening of the lower troposphere is necessary to trigger the convective phase of a Madden–Julian oscillation (MJO). However, the relative importance of the processes controlling this moistening has yet to be quantified. Among these processes, the importance of the moistening by shallow convection is still debated. The authors use high-frequency observations of humidity and convection from the Research Vessel (R/V) *Mirai* that was located in the Indian Ocean ITCZ during the Cooperative Indian Ocean Experiment on Intraseasonal Variability/Dynamics of the MJO (CINDY/DYNAMO) campaign. This study is an initial attempt to directly link shallow convection to moisture variations within the lowest 4 km of the atmosphere from the convective scale to the mesoscale. Within a few tens of minutes and near shallow convection occurrences, moisture anomalies of 0.25–0.5 g kg^{-1} that correspond to tendencies on the order of 10–20 g kg^{-1} day^{-1} between 1 and 4 km are observed and are attributed to shallow convective clouds. On the scale of a few hours, shallow convection is associated with anomalies of 0.5–1 g kg^{-1} that correspond to tendencies on the order of 1–4 g kg^{-1} day^{-1} according to two independent datasets: lidar and soundings. This can be interpreted as the resultant mesoscale effect of the population of shallow convective clouds. Large-scale advective tendencies can be stronger than the moistening by shallow convection; however, the latter is a steady moisture supply whose importance can increase with the time scale. This evaluation of the moistening tendency related to shallow convection is ultimately important to develop and constrain numerical models.

1. Introduction

A coordinated international campaign occurred during the boreal winter of 2011/12 over the Indian Ocean. Its goal was to monitor and understand the physical processes that lead to the triggering of large-scale organized convective perturbations that characterize the Madden–Julian oscillation (MJO; e.g., Zhang 2005; Yoneyama et al. 2013). This campaign, the Cooperative Indian Ocean Experiment on Intraseasonal Variability/Dynamics of the MJO (CINDY/DYNAMO) campaign, consisted of several projects, including CINDY2011, DYNAMO, the Atmospheric Radiation Measurement Program (ARM) MJO Investigation Experiment (AMIE), and the Littoral Air–Sea Process (LASP) experiment. The observed increase of moisture in the lower troposphere prior to the triggering of the convectively active phase of

Corresponding author address: Hugo Bellenger, Japan Agency for Marine-Earth Science and Technology, 2-15 Natsushima-Cho, Yokosuka-city, Kanagawa 237-0061, Japan.
E-mail: hbellenger@jamstec.go.jp

DOI: 10.1175/JAS-D-14-0042.1

the MJO (Johnson et al. 1999; Kemball-Cook and Weare 2001; Benedict and Randall 2007; Thayer-Calder and Randall 2009; Riley et al. 2011; Cai et al. 2013) is one of the fundamental features to be studied with this campaign. The importance of this preconditioning for deep convection associated with the MJO has been stressed by many observational (e.g., Johnson et al. 1999; Kikuchi and Takayabu 2004; Holloway and Neelin 2009) and modeling studies (e.g., Zhang and Song 2009; Cai et al. 2013). A possible consequence of our lack of understanding of the origin of this preconditioning is the limitation of the forecast skill of the timing of the MJO triggering. Indeed, forecast models have problems simulating the evolution from a dry atmosphere to the moist phase (e.g., Agudelo et al. 2006; Nasuno 2013). Note that, in addition to the MJO, the moistening of the lower troposphere may also be important for other phenomena in which deep convection plays a central role, such as mesoscale convective systems (MCSs), synoptic convectively coupled waves (e.g., 2-day waves) (Takayabu et al. 1996), or equatorial convectively coupled Kelvin waves (Straub and Kiladis 2002). All of these phenomena, indeed, share a comparable structure despite their different spatiotemporal scales (Mapes et al. 2006; Riley et al. 2011).

Shallow convection and congestus clouds provide a possible explanation for this preconditioning through the vertical convective transport of moisture from the boundary layer into the lower troposphere (e.g., Johnson et al. 2001; Kuang and Bretherton 2006; Waite and Khouider 2010; Del Genio et al. 2012; Powell and Houze 2013; Xu and Rutledge 2014). However, the role of the moistening by shallow cumulus and congestus has been recently questioned (Hohenegger and Stevens 2013; Kumar et al. 2013). In particular, Hohenegger and Stevens (2013) suggest through bulk computations and large-eddy simulations (LESs) that congestus alone are not sufficient to explain the observed rapid increases in lower-tropospheric moisture. They suggest that this moistening can, however, be attributed to large-scale ascent. Using 7 years of multisatellite measurements, Masunaga (2013) showed that, away from organized convection, vertical moisture flux through the cloud base is the principal source of free-tropospheric moistening. This vertical flux is partly due to large-scale updraft and partly due to convective eddies (shallow cumulus and congestus clouds). They further showed that a few hours prior to organized convection, the large-scale updraft term increases to be the primary source of free-tropospheric moisture before being dominated by horizontal moisture convergence. From these results, Masunaga (2013) concludes that congestus eddy moistening is unlikely to be a major mechanism for preconditioning deep convection on the scale of a day. However, uncertainties remain in the evaluation of the large-scale mean updraft and convective updrafts terms. In addition, Masunaga (2013) notes that these conclusions may not hold for longer time scales, such as that of the MJO. Indeed, in a case study of boreal summer intraseasonal variability over Palau (in the western Pacific Ocean), Katsumata et al. (2013) used sounding network–derived moisture budgets to show that both convective-scale and large-scale processes are major contributors to lower-troposphere moistening prior to the triggering of deep convection; this could also be the case for the boreal winter MJO over the Indian Ocean.

The quantification of convective moisture transport has been the subject of previous studies using models (e.g., Waite and Khouider 2010; Hohenegger and Stevens 2013), satellites (Zelinka and Hartmann 2009; Masunaga 2013), or sounding networks (e.g., Nitta and Esbensen 1974; Schumacher et al. 2008; Katsumata et al. 2013). Notably, these different indirect approaches all lead to a shallow convection–associated moisture tendency on the order of 1–2 $g\,kg^{-1}\,day^{-1}$. This study is the first attempt to directly quantify the moisture tendencies linked with shallow convection from field observations. This diagnostic is conducted at various scales. We will first diagnose the local and instantaneous moisture tendency in the direct vicinity of the cloud (a few tens of minutes and a few kilometers) before evaluating the moisture tendency on the mesoscale (a few hours and 10–100 km). Thus, we take advantage of the collocated high-frequency observations of cloud populations by C-band-scanning Doppler radar and lower-tropospheric moisture profiles by a high-spectral-resolution lidar (HSRL) onboard the Research Vessel (R/V) *Mirai*. For technical reasons that will be discussed in the following sections and owing to the nature of the convection that was observed by R/V *Mirai* during CINDY/DYNAMO, we will focus on situations characterized by shallow convection and its impact on moisture variation below 4 km during nighttime. It has yet to be noted that the lower troposphere is where the moisture variations are the most likely to influence convection (e.g., Jensen and Del Genio 2006; Holloway and Neelin 2009). In the next section, we present the data that are used in this study and the approach to quantify the humidity variations associated with shallow convection. Section 3 presents the results of our analysis, and section 4 provides a summary and discussion.

2. Data and methods

This study is based on the measurements from the CINDY/DYNAMO campaign that was conducted over the near-equatorial Indian Ocean from October 2011 to March 2012 [see Yoneyama et al. (2013) for a description of the campaign]. Here, we focus on the observations

from the special observing period (SOP; 1 October–28 November) while the station of the R/V *Mirai* was nominally located at 8°S, 80.5°E. In this study, moisture is observed using the Raman lidar technique and 3-hourly sounding data, and convection is characterized using the R/V *Mirai* C-band Doppler radar and onboard ceilometer. We provide details of these data, which are available online (http://www.jamstec.go.jp/iorgc/cindy/obs/obs.html), in the following sections. We then present the compositing approach used for deriving the in situ moisture variations associated with shallow convection and the approach to diagnose the large-scale tendencies.

a. CINDY/DYNAMO observations

We use observations from Vaisala RS92-SGPD sondes that were launched every 3 h from R/V *Mirai*. The sounding observations were processed using Vaisala software (V3.64), which contains a built-in correction for solar radiation dry bias and time-lag errors at cold temperatures. The correction of these errors results in accurate moisture fields, even in the upper troposphere, where these corrections are largest (Ciesielski et al. 2014). We then interpolate the sounding observations to obtain a 90-m vertical resolution dataset.

The vertical distribution of water vapor is also monitored using a water vapor Raman lidar technique (e.g., Sakai et al. 2003). The receiver system to measure the water vapor Raman backscatter signal at 660 nm is added to an HSRL onboard the R/V *Mirai* (Nishizawa et al. 2012). The deduced water vapor density ($g\,m^{-3}$) is only evaluated during nighttime (between 1500 and 2300 UTC) because of the insufficient signal-to-noise ratio during daytime. The vapor density is observed every 1 min with a vertical resolution of 3.75 m. We first remove the HSRL data with low signal-to-noise ratios and data contaminated by clouds and rain. We then divide the water vapor density by the sounding's mean air density profile to convert it into water vapor mixing ratio ($g\,kg^{-1}$). Figure 1a shows the vertical distribution of the water vapor mixing ratio measured by HSRL (colors) and by the sondes (black dots). The HSRL mixing ratios remain mainly within the range of the sounding measurements up to 4 km. Yet at any height and despite a strong signal-to-noise ratio, some evidently erroneous values of the water vapor mixing ratio are retrieved from the HSRL. For each altitude, we only consider HSRL-derived mixing ratios that fall within the interval defined by the minimal and maximal values observed by the R/V *Mirai* sondes for the SOP two legs. Figure 1b shows the proportion of HSRL data that are removed as a function of height (black line). This proportion is low below 4 km (approximately 5%), but more than 50% of the HSRL data are rejected for being outside the reasonable range above 5 km. Then we keep the full 1-min time resolution of the HSRL data but average them over 90 m in the vertical.

To discuss the accuracy of the HSRL-derived water vapor mixing ratio, we compare the 1-min HSRL mixing ratio to the collocated sounding observations and report statistics in Fig. 1. Figure 1c shows the mean and standard deviation of the relative difference between the HSRL and sonde water vapor mixing ratios. Following Sakai et al. (2007), this relative difference is defined as (HSRL − sonde)/[(HSRL + sonde)/2] and is expressed as a percentage. The mean relative difference is less than +5% up to approximately 3.5 km. It then rapidly increases and reaches +20% at 4 km. The standard deviation of the relative difference increases steadily from approximately 10% below 2 km to 60% at 4 km. This actually corresponds to a constant standard deviation of the difference between the HSRL and sonde mixing ratios of approximately $1.5\,g\,kg^{-1}$ for all heights (not shown). Yet this relative loss in precision with height should not prevent the use of the HSRL mixing ratio observations in monitoring the average variations in moisture between 1- and 4-km heights by a compositing approach. Figure 1b shows the vertical profiles of the correlation coefficients between the HSRL and sonde data: the coefficients are as low as 0.5 above 4 km and below 1 km (despite a low average relative difference). However, the correlation between the two datasets is generally between 0.8 and 0.9 from 1 to 4 km. One can note that this reduced correlation at higher levels may be due to limitation in the Raman lidar technique as suggested by the increase in the number of erroneous data with height (Fig. 1b). This may also be partly due to the horizontal drift of the balloon away from the ship location during its ascent. At a given height, sondes and HSRL techniques would then measure two distinct air parcels.

The cloud population is monitored using the C-band Doppler radar onboard R/V *Mirai*. Reflectivity and Doppler velocity are available on a Cartesian grid with dimensions of 200 km × 200 km (1-km resolution) in the horizontal and 20 km in the vertical (0.5-km resolution) with a temporal resolution of 10 min. Following Katsumata et al. (2008), the radar reflectivity is corrected for attenuation by rain and the atmosphere before being validated using Tropical Rainfall Measuring Mission (TRMM) Precipitation Radar (PR) observations for all overpasses during the cruise. Convective and stratiform features are flagged following the texture-based algorithm of Yuter et al. (2005), which is based on Steiner et al. (1995) using 2-km-height echoes. Local maxima in reflectivity or reflectivity above a certain threshold are flagged as convective. The remaining precipitation echoes are flagged as stratiform. Finally, echo-top heights are

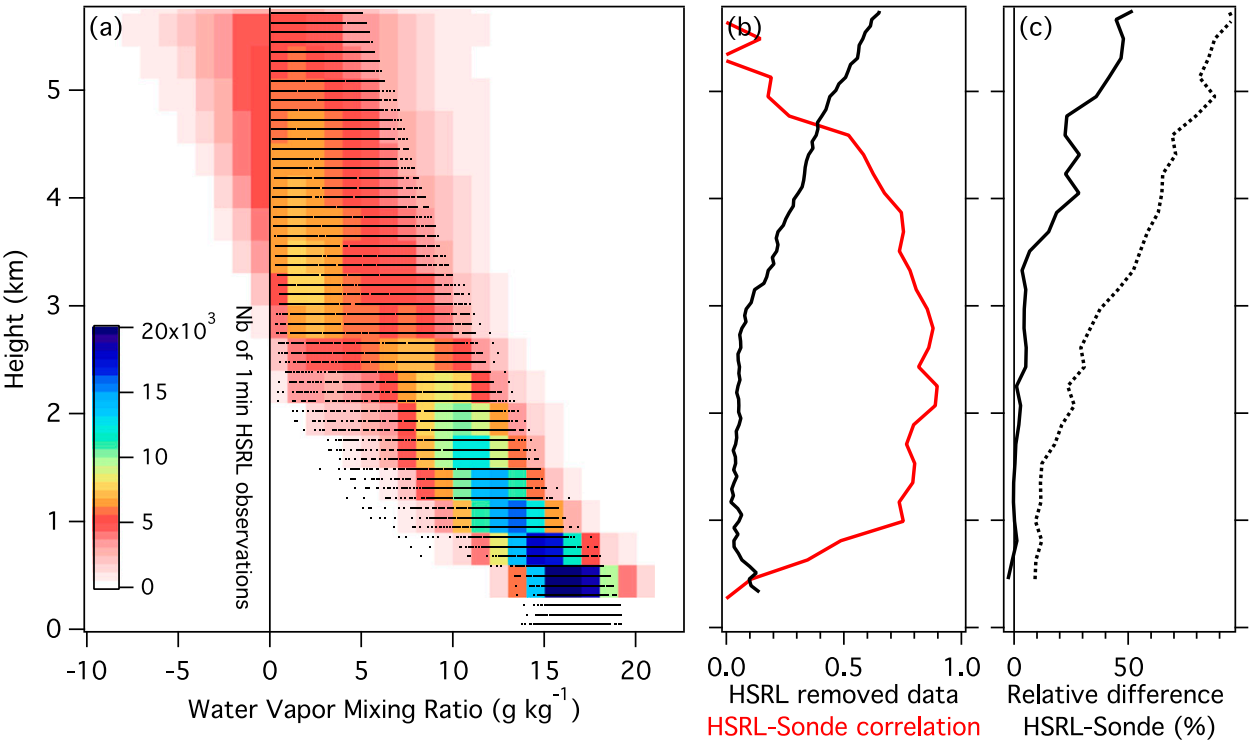

FIG. 1. (a) Distributions of the water vapor mixing ratios (g kg^{-1}) from HSRL (colors) and sounding data (black dots). The HSRL data that are flagged as noisy or cloudy are removed prior to the computation of the distribution. (b) Proportions of HSRL data that are removed for being outside the range of values observed by the sounding (black) and the correlation between the remaining HSRL and collocated sounding data (red). (c) Mean relative difference between the HSRL and sounding data (solid) and the corresponding standard deviation (dashed). The relative difference is defined as (HSRL − sonde)/[(HSRL − sonde)/2].

defined here as the top of the first cloud layer using a 10-dBZ threshold by scanning the observed volume upward. To detect the presence of clouds in the direct vicinity of R/V *Mirai*, we also use 1-min ceilometer observations of the cloud-base height (with a 30-m vertical resolution).

b. *In situ moisture variation composites*

The main issue that we face in linking convective clouds with changes in humidity is the lack of collocated observations of moisture profiles and vertical structures of clouds. No vertically pointing cloud radar data are available at the present time from R/V *Mirai*, and the C-band radar produces volume scans with a maximum elevation of 40°. Thus, no radar observations are available directly above R/V *Mirai*, and the full-troposphere observation is done for distances of at least 20 km from the ship. It is thus not possible to determine the depth of the clouds that are passing over R/V *Mirai*, nor is it possible to associate an observed moisture variation with a particular type of convection. Therefore, it is necessary to link moisture variations and convection depth on a statistical basis. Here, we use (i) the C-band radar data to characterize the convection around the research vessel and (ii) the ceilometer-derived cloud-base height to select time steps that correspond to convection occurrence over R/V *Mirai*:

(i) The radar observations are used to characterize the convection around the research vessel. Johnson et al. (1999) showed that tropical convection can be roughly separated into three categories: shallow cumulus with echo-top heights below 4 km, congestus with echo-top heights between 5 and 9 km, and cumulonimbus with echo tops above 10 km. Zuluaga and Houze (2013), Rowe and Houze (2014), and Xu and Rutledge (2014), using CINDY/DYNAMO data, and Riley et al. (2011) and Barnes and Houze (2013), using *CloudSat* and TRMM observations, showed that all types of convective clouds can be observed during all phases of the MJO and that their relative proportions change with time. Any radar scene is thus likely to be a mix of convective clouds that certainly have different impacts on their environmental moisture: shallow convection is likely to moisten the first few kilometers of the atmosphere, whereas deep convection tends to dry it (e.g., Schumacher et al. 2008). Therefore, in an attempt to define the scene's most representative convective cloud type, we characterize each 10-min

radar scene by the mean echo-top heights z_m of echoes classified as convective in the 200 km × 200 km region covered by the radar. Then we define each 10-min radar observation with $z_m \leq 4$ km as shallow convection scenes.

(ii) To capture moisture changes linked with convective activity, we must determine when convection is actually occurring at the R/V *Mirai* position; thus, we use observations from the ceilometer. Convective clouds are characterized by low cloud bases (e.g., Takayabu et al. 2006), and we therefore consider that convection is occurring above R/V *Mirai* when clouds with base heights below 1.2 km are detected. Convective cloud cover is simply defined as the percentage of clouds detected by the ceilometer with bases below 1.2 km. For shallow convection situations as defined from the C-band radar observations [see (i)], the convective cloud cover is on the order of 10%, on average. The average duration of continuous convective clouds above R/V *Mirai* is 1.9 min (with a 1.8-min standard deviation), and 80% of the durations are shorter than 3 min. On the other hand, the average duration between two convective clouds is approximately 30 min (with an 80 min standard deviation), and approximately 75% of the durations are longer than 3 min. Hence, the shallow convective clouds appear as isolated 1–3-min events separated by larger periods without convective clouds.

Using the radar and ceilometer information, we construct time–height composites of moisture following one of two methods, depending on the scale of interest:

- To focus on instantaneous and then local scales, we use all ''convective clouds'' (cloud bases below 1.2 km) detected for at least two successive minutes during shallow convection situations. The zero lag is taken as the time center of the convective cloud. We only consider convective occurrences during nighttime when HSRL data are available (1500–2300 UTC). The composite is then performed on the convective cloud–free time period around each retained convective cloud to avoid combining the information on neighboring convective occurrences. To increase the composite significance while keeping a sufficient time resolution to resolve rapid variations of moisture, we compute the composite with averages over 3-min time steps from the 1-min HSRL data.
- To focus on mesoscale moisture variations, we use local maxima in shallow convective cloud cover computed over 30 min or 3 h to compare HSRL to sounding data; we then construct composites in between these maxima using 30-min and 3-h time steps, respectively. For the 3-h composites, we only retain maxima that correspond to a convective cloud cover of at least 5%.

We use the Student's t test to determine whether the obtained mean moisture anomalies are significantly different from zero. To evaluate the number of degrees of freedom, we simply assume that all the convective events that are averaged are independent, as the time slices that are used do not overlap with one another. For each composite, the number of degrees of freedom, which decreases away from lag 0, is shown in the figure caption. Then, we evaluate the moisture tendencies at each height by fitting a straight line using the least squares method. Of course, the obtained tendencies are sensitive to the time interval chosen to compute the linear regression. We select this interval to be centered on lag 0 (convection occurrence), and its extent is fixed to capture statistically and physically significant moisture anomalies. This interval changes depending on the time resolution of the considered composite (3 min, 30 min, or 3 h). The choice of the time interval and its influence on the obtained tendencies is specified for each particular case in the results section. The HSRL data are only available during nighttime; thus, to present consistent results, we consider only nighttime soundings/radar and reanalysis data to construct the corresponding composites. However, taking into account both night and day does not change the order of magnitude of the diagnosed moisture variations, nor does it change our conclusions.

Note that if C-band radar captures well the amount of precipitating shallow convective clouds, it underestimates nonprecipitating shallow convection (e.g., Feng et al. 2014). Note also that, if the C-band radar data used to define the shallow convective scenes may underestimate the amount of nonprecipitating clouds, then the composites are based on ceilometer observations. Therefore, we take into account both precipitating and nonprecipitating clouds in our analysis. Furthermore, some echoes classified as ''stratiform'' correspond to echo tops lower than the freezing level (approximately 5-km height). Such echoes should, in fact, be classified as shallow convection. Thus, we certainly underestimate the number of scenes for which shallow convection is the dominating feature. However, our goal here is to avoid selecting scenes with too many high congestus clouds or deep convective clouds. So the underestimation of shallow convective features leads us to consider only the most clearly shallow convective scenes. Yet some deeper convective clouds can pass over R/V *Mirai* when it is mainly surrounded by shallow convection. Thus, we possibly combine these deeper clouds with the shallow convective cases in our composite. Congestus clouds are thought to mainly detrain at approximately 5–6 km and

to have weak impact on the moisture below 4 km (e.g., Schumacher et al. 2008). Furthermore, deeper cumulonimbi tend to dry the lower troposphere (Schumacher et al. 2008). Thus, the inclusion of deeper cloud cases in our shallow convection composites would lead us to underestimate the moistening of the lower troposphere associated with shallow cumulus clouds. We tested the sensitivity of our approach to the mean echo-top-height threshold to define shallow convective scenes and to the radar area used to compute this mean echo-top height. The composited moisture anomalies and the associated moisture trends are sensitive to these choices. However, they exhibit comparable orders of magnitude (not shown).

c. *Large-scale moisture tendencies*

We also use the Interim European Centre for Medium-Range Weather Forecasts (ECMWF) Re-Analysis (ERA-Interim; Dee et al. 2011) to compare the local variations of humidity with large-scale tendencies. The use of ERA-Interim is justified by the high correlation between the reanalysis and R/V *Mirai* sounding moisture below 10 km (linear correlation coefficient of approximately 0.85). The large-scale moisture tendencies are computed every 6 h following Trenberth (1991) and averaged on a $2° \times 2°$ box centered on the position of R/V *Mirai*. This box is chosen to have comparable size as the region covered by the R/V *Mirai* radar. The moisture budget is computed from its advective formulation:

$$\frac{\partial q}{\partial t} = -\mathbf{v}\nabla\mathbf{q} - \omega\frac{\partial q}{\partial p} - \frac{Q_2}{L}, \tag{1}$$

where the $-Q_2/L$ term is computed as a residual [condensation minus evaporation and transport by unresolved eddies; Yanai et al. (1973)], $\mathbf{v}$ is the horizontal wind, and ω is the vertical velocity ($\mathrm{Pa\,s^{-1}}$). The time- and space-centered derivatives are computed before averaging over space. The fields are not filtered over time, as strong variations of humidity can occur on very short time scales (e.g., Powell and Houze 2013). As noted previously, for each 6-h moisture trend, the type of convection is characterized by the 6-h convective z_m values observed by the R/V *Mirai* radar. In particular, shallow convective situations are defined as 6-h periods in which $z_m \leq 4$ km. Again, we only provide results for nighttime (1800 and 2400 UTC, corresponding to 2330 and 0550 local time). However, the results are similar when considering daytime time steps.

The mass imbalance (model errors and interpolation on standard pressure levels) can be diagnosed by the residual r of

$$\nabla\mathbf{v} + \frac{\partial\omega}{\partial p} = r; \tag{2}$$

the ratio of the RMS of r above the RMS of the horizontal divergence quantifies the relative error of the mass budget (Trenberth 1991). This relative error is approximately 25% below 200 hPa (not shown). Both the ERA-Interim vertical velocity and the vertical velocity deduced from horizontal divergence will thus be used to assess the uncertainty of the computed vertical advection.

3. Results

a. *Convective activity observed by R/V* Mirai *during CINDY*

Figure 2 shows the time series of the distributions of the echo-top heights for convective clouds observed by the R/V *Mirai* radar together with the sounding's water vapor mixing ratio anomalies relative to the mean of the two legs. After the first convective event at the beginning of October, the convective activity remains weak with echo tops mainly below 6 km (Fig. 2). The convection is relatively more active throughout November, with short periods that are characterized by clouds reaching approximately 12-km heights. The stronger signal of humidity is found below 8 km, with a link between cloudy periods and moist periods. The correlation coefficients between the convective cloud-top distribution and mixing ratio for each altitude are computed as 0.4–0.5 from 1- to 8-km heights. As also stated by Yoneyama et al. (2013) and Johnson and Ciesielski (2013), there is no clear increase in convective activity associated with the active MJO phase at the end of October (at least when R/V *Mirai* was on site) and at the end of November, whereas it does increase over the northern part of the Indian Ocean. R/V *Mirai* was indeed located south of the region where two MJO events were triggered during the SOP [see Fig. 13 of Yoneyama et al. (2013)], and it mainly sampled scenes characterized by shallow convection. Thus, the R/V *Mirai* observations are suitable to focus on the impact of shallow cumulus clouds on the moisture in the lower troposphere.

A simple way to obtain a synthetic view of the observed cloud distribution characteristics is to use the distribution of the number of radar scenes as a function of convective and stratiform mean echo-top heights (Fig. 3a). R/V *Mirai* mainly monitored scenes with shallow convection mean echo tops lower than 5 km. Note that most echoes flagged as stratiform with diagnosed echo-top heights below the freezing level (approximately at 5 km) should be interpreted as shallow convection, as discussed in the previous section. Some periods are,

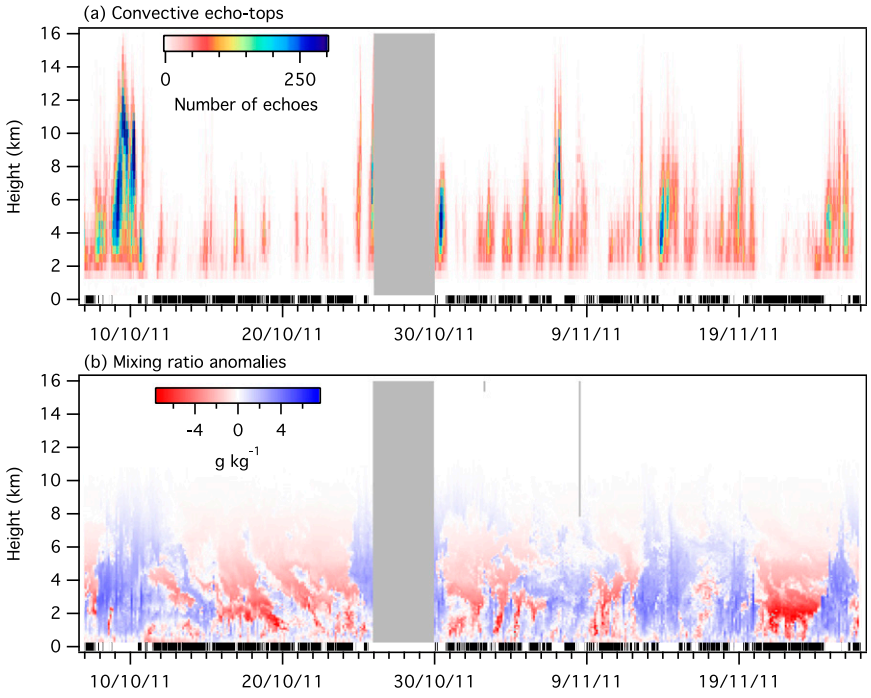

FIG. 2. Time–height distribution of (a) convective echoes observed by the C-band radar onboard R/V *Mirai* for the period 7 Oct–26 Nov 2011 and (b) 3-hourly sounding mixing ratio anomalies from the mean of the two SOP legs. The gray shading shows the period when R/V *Mirai* was not at its position between legs 1 and 2 of the SOP. The 10-min time steps corresponding to shallow convection situations are also indicated with black ticks at the bottom of each panel.

however, characterized by higher convective echo tops. In particular, there is a secondary maximum of the number of scenes with mean convective and stratiform echo tops at approximately 6–7 km. In Fig. 3a, we reported (vertical dashed lines) the intervals chosen to define the three main convective cloud categories following Johnson et al. (1999). Figure 3b shows the mean distributions of the convective echo tops and the associated standard deviations for the situations sorted according to z_m. Despite the shallow convection underestimation by the radar, 60% of the scenes are characterized by mostly shallow convection ($z_m \leq 4$ km). This type of scene corresponds to shallow cumuli and shallower congestus (Fig. 3b). Additionally, 38% of the situations have mainly congestus clouds ($4 < z_m \leq 8$ km). Finally, deep convective cases account for 2% of the situations. Shallow convective clouds occur in the three categories of scenes, but it is clear that for $z_m \leq 4$ km, the convective cloud population is unambiguously dominated by shallow convection.

The relative humidity profiles corresponding to the three convective cloud categories are presented in Fig. 3c. The mean RH profiles show a large spread comparable with that found by Holloway and Neelin (2009) when sorting the profiles by column water vapor rather than rainfall (see their Fig. 4b). This suggests a link between the echo-top distribution and the water vapor column (mainly the lower-free-troposphere moisture). The shallow convective situations are associated with a very dry troposphere (relative humidity of less than 40%) above 3 km (Fig. 3c). This may explain the limitation of the convective cloud-top height (e.g., Jensen and Del Genio 2006). The main difference in the mean relative humidity profiles between shallow convective and congestus cases can be seen at heights of approximately 3–5 km. Finally, for deep convective cases (up to 10 km), the upper troposphere clearly has a higher relative humidity. In addition to a drier troposphere, shallow convective cases were also characterized with higher stability in the ~2–3-km layer (not shown), with vertical temperature gradients from approximately -3.5 to -4 K km^{-1} on average, whereas congestus situations have a gradient of approximately -5 K km^{-1}. This could also contribute to the limitation of the vertical extension of the clouds (e.g., Zuidema 1998; Davison et al. 2013).

b. *Instantaneous moisture variations associated with shallow convection*

In this section, we analyze the local and instantaneous moisture anomalies and tendencies in the vicinity of

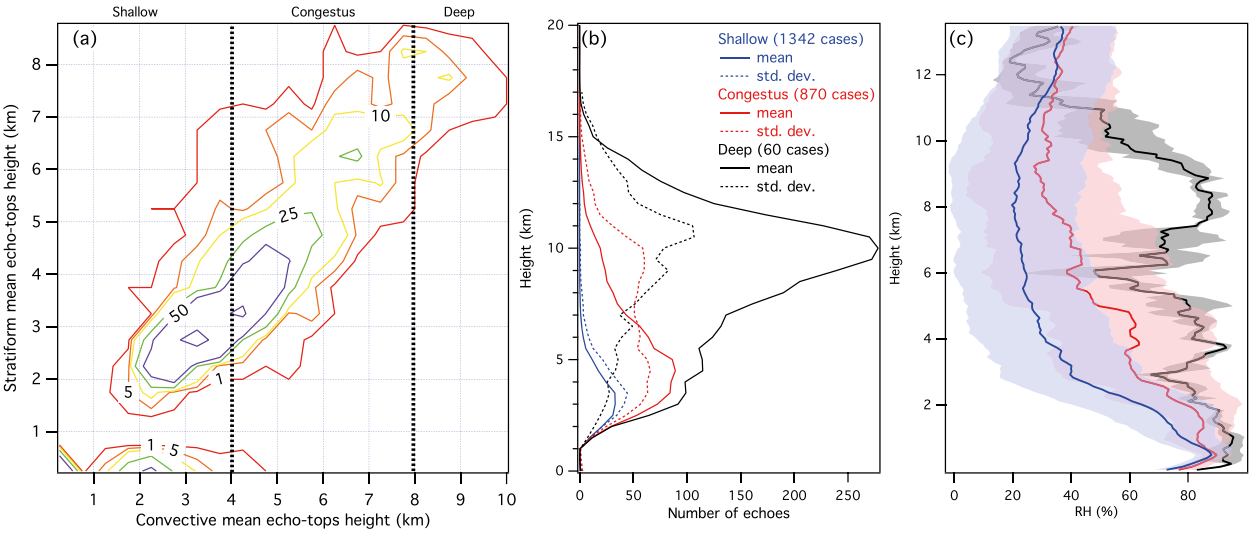

FIG. 3. (a) Number of radar-observed scenes as a function of the mean echo-top heights for echoes classified as convective (abscissa) and stratiform (ordinate); (b) mean vertical distribution (solid) and standard deviations (dashed) of the number of convective echo tops for the mean convective echo-top height below 4 km (shallow convection scenes; blue), between 4 and 8 km (congestus scenes; red), and above 8 km (deep convection scenes; black); and (c) mean relative humidity (%; standard deviation is shaded) for the same three scene categories. The number of scenes in each category is also reported in (b). The three category boundaries are reported in (a) (vertical dashed lines). Note that only nighttime data were used to create this figure.

shallow convective clouds (cloud base below 1.2 km and mean convective echo-top height below 4 km). Figure 4a shows the composited moisture anomalies derived from 1-min HSRL nighttime observations associated with the occurrence of shallow convective clouds. Despite averaging over three time steps and the relatively large amount of cases used to construct the composite, the composite remains noisy. Yet a significant moist anomaly of more than 0.2–0.5 g kg^{-1} is observed below 1 km from the 0.5 h prior to the convection, and it disappears gradually after lag 0. Between 1 and 4 km, a comparable moist anomaly appears slightly before lag 0 and remains until it dissipates around lag +0.25 h. This feature could suggest a net upward transport of moisture from the first kilometer of the boundary layer to the 1.5–4-km-height layer by the convection occurring around lag 0. In addition, cold pools can also be associated with comparable moisture anomalies in the boundary layer (Zuidema et al. 2012).

To understand the link between these anomalies and the shallow convective clouds, we must consider the associated horizontal wind profiles. Shallow convective clouds mainly detrain on their downshear side (Telford and Wagner 1980; Perry and Hobbs 1996). The downshear side is simply the direction the vertical shear vector $\partial\mathbf{w}/\partial z$ points. Here, the wind tends to be stronger below 1 km than between 1 and 4 km (Fig. 5a). Therefore, an active convective cloud should be tilted so that, as observed from the ship, its summit follows its base [see Fig. 17b of Perry and Hobbs (1996)]. Then the detrained moisture or "halo" should also follow the convective base [see Fig. 18 of Perry and Hobbs (1996)]. In Fig. 5b, we plotted the normalized distribution of the vertical shear between 0.5 and 4 km corresponding to each shallow convective situation. The vertical shear considered here is the projection of the 0.5–4-km vertical shear vector in the direction of the 0.5–4-km mean wind. For most of the cases, the vertical shear is negative. Thus, the mean wind and the vertical shear often have opposite signs. Neglecting the cloud's propagation and assuming that it is mainly advected by the mean wind, the downshear side of the cloud tends to pass above the ship after the cloud base. This result corresponds to a positive lag between the observation of the convective cloud base and the 1–4-km-height positive moisture anomaly passing over the vessel, as observed on the average (Fig. 4a).

Figure 4a also shows the mean evolution of the convective cloud cover from the ceilometer. Away from lag 0, the mean convective cloud cover quickly drops to less than 20%. Convective clouds are observed by the ceilometer for 2 min (±2 min) on average (see previous section). Between 0.5- and 4-km heights, the wind speed is 5 m s^{-1} (±2.5 m s^{-1}) on average (Fig. 5b). Thus, the horizontal scale is approximately 0.5–1 km for each convective cloud. In comparison, the impact of the cloud on the moisture field above 1 km remains statistically significant for approximately 12 min. Thus, the horizontal scale is approximately 3.5 km (±1.7 km) for the moisture anomaly and is approximately 4–5 times larger than the convective cloud extent. Yet the moisture halo is usually a similar

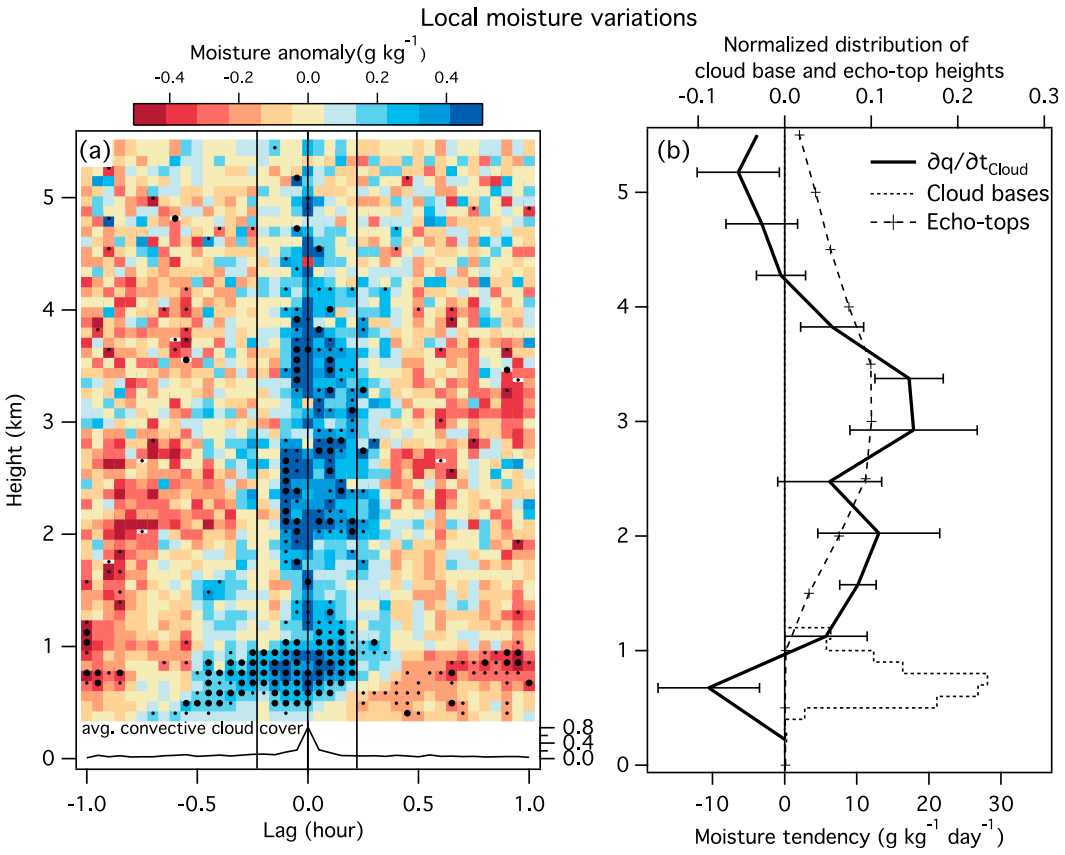

FIG. 4. (a) Time–height composites of HSRL mean moisture anomalies (colors; $g\,kg^{-1}\,day^{-1}$) around shallow convective cloud occurrences of at least 2 min (260 cases): the small (large) dots show where the anomalies are different from zero at the 95% (99%) level (the number of degrees of freedom varies from 50 to 160 close to lag 0), and the black curve (above the abscissa) is the mean convective cloud cover (proportion of clouds with cloud-base height lower than 1.2 km using the ceilometer). (b) Mean instantaneous moisture tendency profile ($\partial q/\partial t_{\text{Cloud}}$; solid thick line) associated with shallow convective cloud occurrence. This tendency is computed from (a) on a 25-min interval centered on lag 0 [time interval highlighted in (a) by vertical lines] and vertically averaged every 500 m (the error bars are the standard deviation of the moisture tendencies within each 500-m bin). Also superimposed is the normalized distribution of the ceilometer cloud-base heights lower than 1.2 km (dotted) and radar convective echo tops (dashed with plus signs).

magnitude to the cloud radius and rarely reaches 4 times its value, even in strong wind shear conditions (Perry and Hobbs 1996; Laird 2005). This discrepancy may arise from the fact that previous studies of humidity halos considered isolated clouds, which is not necessarily the case here. In addition, our estimate of the horizontal scale of clouds is based on the assumption that these clouds are simply advected by the mean wind. However, active convective clouds can propagate at a speed that is roughly equal to the difference of the wind below and above the cloud base (Telford and Wagner 1980). Here, this mean speed difference is approximately $2\,m\,s^{-1}$ on average (Fig. 5a). Thus, adding this propagation speed to the mean advection speed leads to an average cloud extent of about 1 km.

Figure 4b further shows the moisture tendency profile associated with shallow convection. It is computed based on the mean moisture anomalies within ±12 min (Fig. 4a). Shallow convection is associated with drying below 1 km on the order of $-10\,g\,kg^{-1}\,day^{-1}$ and moistening on the order of $10–20\,g\,kg^{-1}\,day^{-1}$ between 1.5 and 4 km. Such strong tendencies on such a short time scale suggest that rapid processes, such as convection, are at work here. For this reason, this tendency is noted as $\partial q/\partial t_{\text{Cloud}}$ on Fig. 4b and herein. Further analysis (see section 3d) will show that indeed large-scale advections act on a slower time scale. Interestingly, the strong near-surface drying corresponds to the maximum of the cloud-base height distribution at approximately 600 m. Above 1.5 km, the strong moistening reaches its maximum at approximately 3 km, which also corresponds to the top of the stable layer (not shown) and to the maximum of the shallow convective echo-top distribution (Fig. 4b), where

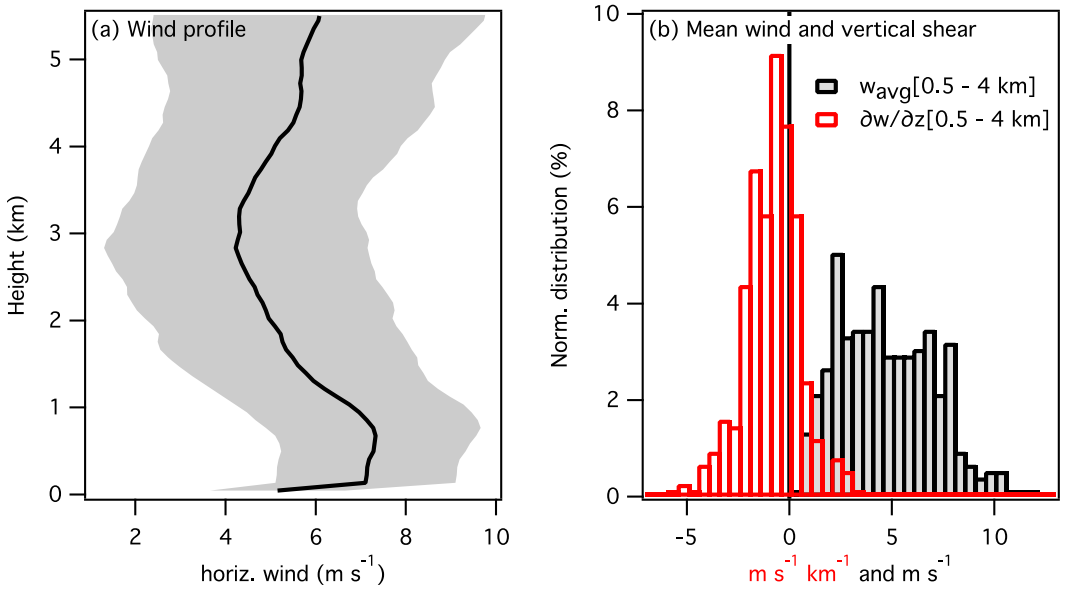

FIG. 5. (a) Mean horizontal wind speed profile for shallow convective situations; the standard deviation is represented by the gray shading and (b) mean wind (black) and vertical wind shear (red) distributions over 0.5–4-km heights. The vertical wind shear is computed from the linear fit of the horizontal wind vector as a function of height using the least squares method and is projected on the 0.5–4-km-height mean wind direction.

most of the detrainment is likely to occur. Note that changing the time interval from ±9 to ±15 min does not change the order of magnitude of the moisture tendency (not shown). Note also that the moisture tendency reported here is an evaluation of the local and instantaneous tendencies at the shallow convective cloud scale. The tendency is approximately 10 times stronger than previous estimates (e.g., Waite and Khouider 2010; Hohenegger and Stevens 2013), which provided diagnostics of the moisture tendencies on a larger scale. In the following section, we discuss moisture tendencies on the mesoscale and their links with the local and instantaneous tendencies presented here.

c. *Mesoscale moisture tendencies*

The previous section focused on local moisture tendencies in the direct vicinity of shallow convective clouds. In this section, we aim to evaluate moisture anomalies and tendencies linked with shallow convective clouds on the mesoscale (from 10 km to several hundred kilometers). For each time step, we evaluate the size of the region where shallow convection occurs using the mean distance between convective echoes. An example of an observed shallow convective scene is provided in Fig. 6. The radar reflectivity shows convective echoes with most of the echo tops below 4 km and that spread over a region with a characteristic scale of 60 km. Shallow convection typically spreads over regions with equivalent radii ranging from 20 to 100 km and a mean equivalent radius of approximately 60 km, which is characteristic of the mesoscale. Note that the evaluation of the cluster extensions is, however, limited by the range of the projected radar data (200 km × 200 km). Because the mean wind in the lower troposphere is approximately 5 m s^{-1}, 20–100-km regions should correspond to moisture anomalies on the time scale of approximately 1–5 h. Figure 7a shows the 30-min averaged composite of the moisture anomalies based on the nighttime HSRL data. A distinct 0.25–1 g kg^{-1} moist anomaly is visible up to 4 km after lag 0. It lasts at least until +5 h and thus corresponds to mesoscale anomalies. Figure 8 shows the associated evolution of the convective echo-top distributions. The ceilometer-derived convective cloud cover quickly decreases away from lag 0 (Fig. 7a), whereas there is clearly a statistically significant positive anomaly of the number of shallow convective clouds from −1 to +5 h (Fig. 8). Thus, the moist anomaly shown to persist for a few hours (Fig. 7a) may be linked with the surrounding shallow cloud population, as also observed by Powell and Houze (2013).

Figure 7b shows the mean moisture tendencies computed at ±5.5 h. Note that changing the time interval to ±5 or ±6 h does not change the order of magnitude of the moisture tendency (not shown). The moisture tendency profile of approximately 2–4 g kg^{-1} day^{-1} between 2 and 4.5 km can be compared to the tendencies simulated by Waite and Khouider (2010, their Fig. 6). We can also compare this tendency profile with the

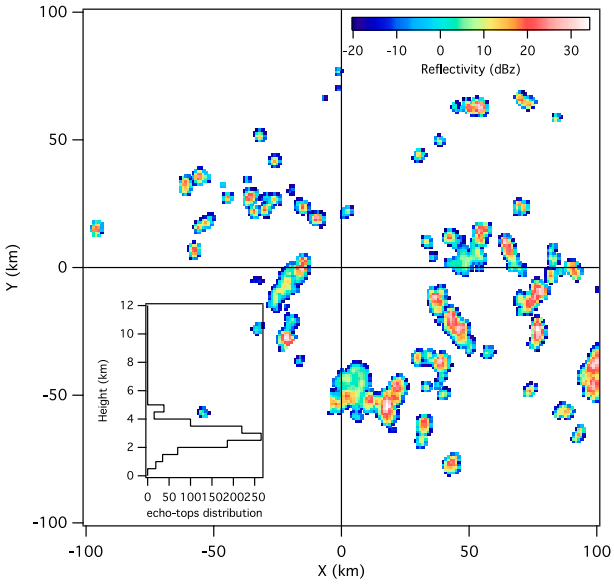

FIG. 6. Example of a shallow convective scene observed by the radar onboard R/V *Mirai*; reflectivity at 2-km height (dB*Z*; colors) and distribution of convective echo tops as a function of height (inset; black line). The size of the region where shallow convection occurs is approximated by the average distance between convective echoes and is here 60 km.

resultant on the mesoscale of the local and instantaneous mean moisture tendencies $\partial q/\partial t_{\text{Cloud}}$ (Fig. 4b). If the observed mesoscale moisture tendency is actually due to shallow convection, then we should obtain:

$$a\partial q/\partial t_{\text{Cloud}} \approx \partial q/\partial t_{\text{Mesoscale}}, \qquad (3)$$

where a is the mean convective cloud cover. Of course, $a\partial q/\partial t_{\text{Cloud}}$ depends on the value of a. Figure 7b shows that the simple relationship of Eq. (3) seems to hold when taking the average convective cloud cover at lag 0. This suggests that the mesoscale moisture tendency (Fig. 7b, thick solid line) can be interpreted as the resultant on the mesoscale of the ensemble of local moisture tendencies associated with shallow convective clouds (Fig. 4b). The relationship expressed by Eq. (3) with a convective cloud cover of approximately 10%–20% would indeed explain the difference between the local moisture tendencies $\partial q/\partial t_{\text{Cloud}}$ of approximately 10–20 g kg^{-1} day^{-1} (Fig. 4b) in the direct vicinity of the cloud and the moisture tendencies of few grams per kilogram per day obtained from bulk analyses or numerical models on larger scales reported in previous studies (Waite and Khouider 2010; Hohenegger and Stevens 2013). Of course, at this scale, horizontal and vertical advections certainly play a role, and we can thus not expect a perfect agreement between the two sides of Eq. (3).

The moisture anomalies associated with the shallow convection shown in Fig. 7a last for several hours. Using 3-h soundings should produce comparable moisture variations. Figure 9a shows the moisture variation composites based on nighttime sounding data. Note that including daytime data does not strongly affect the result. The moisture anomalies that can be observed within 5 h of lag 0 have comparable orders of magnitude (0.5–1 g kg^{-1}) (Fig. 9a). The values are, however, particularly strong and statistically significant below 2 km, whereas they are stronger above 2 km, according to HSRL. Figure 9b shows the mean moisture tendency profile computed at ±7.5 h. According to the sounding observation, the moistening associated with shallow convection peaks at approximately 2 km and is approximately 1–2 g kg^{-1} day^{-1}. Note that below 3 km, this tendency retains the same order of magnitude when computed at ±4.5 or ±10.5 h (not shown). Figure 9b also shows the moisture tendency obtained from composites of 3-h-average HSRL data and the moisture tendencies deduced from local instantaneous tendencies and averaged cloud cover (as in Fig. 7b). The discrepancy between the vertical profile of the mesoscale moisture tendencies diagnosed from the HSRL data (peaking above 2 km) and sounding data (peaking below 2 km) may be partly due to the relatively low temporal resolution of the sounding observations (one every 3 h) and partly due to the relatively small number of maxima of the shallow convective activity used in this analysis (about 35 cases). Despite this discrepancy, comparable moisture tendencies are found from two independent measurements and are on the same order of magnitude as previous estimates (Waite and Khouider 2010; Hohenegger and Stevens 2013). This strengthens the confidence in our direct evaluation of moisture tendencies associated with shallow convective clouds.

d. *Large-scale moisture tendencies*

The large-scale circulation strongly impacts the local moisture budget through horizontal and vertical advection (e.g., Masunaga 2013). Figure 10 shows the SOP mean and standard deviation of the different components responsible for the local moisture tendencies, as described by Eq. (1). These components are computed for nighttime shallow convective situations from the ERA-Interim data on a 2° × 2° box centered on the R/V *Mirai* position. The mean moisture large-scale tendencies (Fig. 10a) and their variability (Fig. 10b) are the same order of magnitude as the tendencies related to convection (although weaker; see Figs. 7b and 9b) and one order of magnitude below the local tendencies (Fig. 4b). This suggests that large-scale advection acts on a slower time scale than convection and that its impact

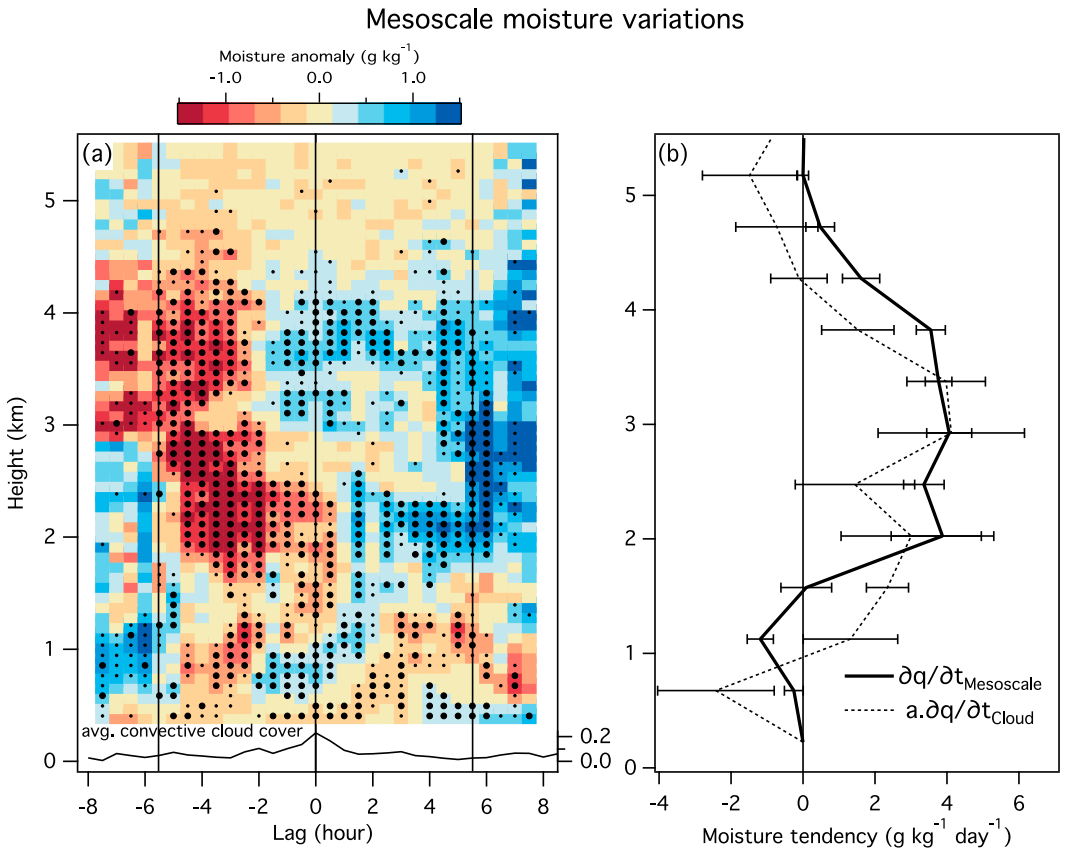

FIG. 7. (a) As in Fig. 4a, the composite of the HSRL moisture anomalies is constructed relative to the maxima in the 30-min convective cloud cover for shallow convection situations (38 cases; see text for details); the number of degrees of freedom is decreasing gradually from 32 close to lag 0 to about 10 at lag ±5.5 h and no data beyond ±8 h. (b) As in Fig. 4b, the mean moisture tendency ($\partial q/\partial t_{\text{Mesoscale}}$; solid) is computed from (a) at ±5.5 h [vertical lines in (a)], and the moisture tendency is evaluated following Eq. (3), with a mean convective cloud cover at lag 0 ($a\partial q/\partial t_{\text{Cloud}}$; dotted line; $a = 23\%$).

can be neglected when considering local instantaneous moisture variations. In other words, local composites (Fig. 4) isolate the effect of shallow convection on lower-tropospheric moisture. On the other hand, mesoscale composites of Figs. 7 and 9 may also contain the effect of advection together with that of convection. The local moisture tendency (thick black line on Fig. 10a) exhibits weak drying when shallow convection is observed. The unresolved processes ($-Q_2/L > 0$ in green) tend to oppose the drying by horizontal advection (in red) and the drying by vertical advection (in blue) because of large-scale subsidence (Fig. 10c). The opposing tendencies are particularly strong below 2 km, where some detrainment of shallow convective clouds can occur (e.g., Nitta and Esbensen 1974). Yet the negative local moisture tendency from ERA-Interim (Fig. 10a) does not correspond to the moistening tendencies observed using HSRL (Fig. 7b) and soundings (Fig. 9b). This could be due to the coarse temporal resolution of the reanalysis data used here (every 6 h). It is interesting to note that, although weaker, the mean apparent moistening term (green in Fig. 10a) resembles the mesoscale moisture tendency from the sounding data (Fig. 9b), with a moistening peaking below 2 km. This raises the question as to how the reanalysis is able to reproduce the effect of shallow convection on lower-tropospheric moisture. Figure 10 also shows the vertical advection tendency computed using the horizontal divergence [Eq. (2)]. This tendency is very close to the direct estimate. We thus verify that, for shallow convective cases, the uncertainty associated with the mass imbalance due to interpolating the modeled vertical velocity on standard pressure levels is small.

Figure 11 shows the time series of the 1–4-km mean horizontal and vertical advections from ERA-Interim and an evaluation of convective cloud moisture transport. The convective cloud moistening is simply diagnosed using Eq. (3), with the mean $\partial q/\partial t_{\text{Cloud}}$ (Fig. 4b) and the convective cloud cover defined as the percentage of time steps with cloud bases below 1.2 km, as observed by the

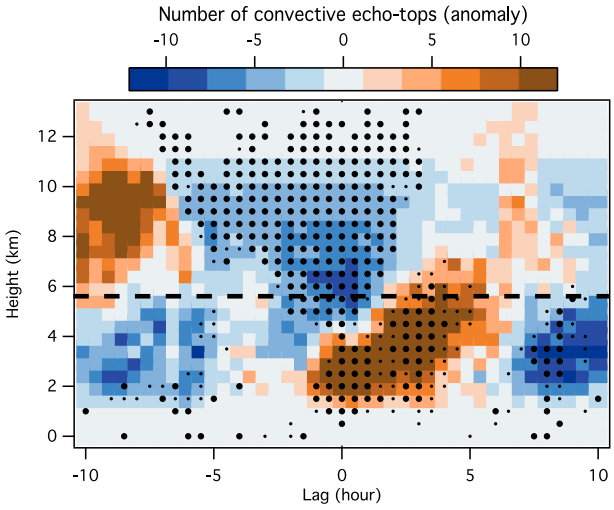

FIG. 8. Time–height composites of the anomalous number of convective echo tops relative to maxima in the 30-min convective cloud cover for nighttime shallow convection situations, as in Fig. 7a. The small (large) dots show where the anomalies are different from zero at the 95% (99%) level (the number of degrees of freedom is between 20 and 38 close to lag 0). The horizontal dashed line corresponds to 5.5-km height for comparison with moisture composites.

ceilometer within 6 h. For consistency, this convective cloud moistening is only evaluated for shallow convection situations, when deeper convection is rare and when convective clouds dominantly detrain between 1 and 4 km. The total number of convective echoes is also reported (bars on the bottom axis). The vertical advection term can reach over ± 5–$6\,\mathrm{g\,kg^{-1}\,day^{-1}}$, which is consistent with the results of Hohenegger and Stevens (2013). These peaks in vertical moisture advection often occur in association with strong convective activity (e.g., 9–10 October), but some strong vertical advection events can also be observed during shallow convection situations (e.g., 15 October). Yet the convective moistening cannot be neglected and is often on the same order of magnitude as the vertical advection (e.g., 16–18 October and 09–11 November) or even stronger (e.g., 11–12 October). The same is true when comparing convective moistening with horizontal advection, which can also reach ± 5–$6\,\mathrm{g\,kg^{-1}\,day^{-1}}$ [e.g., 12 November or during the dry intrusion on 20 November as described by Kerns and Chen (2014)]. Still, horizontal moisture advection and convective moistening may also have the same order of magnitude (e.g., 17 October and 5 November). According to our diagnostic, convective moistening is a relatively steady source of moisture in the 1–4-km layer, whereas the two large-scale advection terms tend to vary rapidly and can change their signs on time scales from approximately 12 h to 2 days. Thus, the advection terms may cancel out when integrated over time, in contrast with the steady moisture source associated with convection. Note that even more shallow convection is observed for deep convective scenes (Fig. 3b) and may also be a local and constant source of moisture for the lower troposphere, particularly throughout the life cycle of an MJO event. This illustrates the potential importance of the moistening associated with shallow convection for synoptic to intraseasonal time scales, as noted in other studies (e.g., Zhang and Song 2009; Waite and Khouider 2010; Katsumata et al. 2013; Powell and Houze 2013; Xu and Rutledge 2014).

4. Summary and discussion

One of the main scientific goals of the CINDY/DYNAMO campaign is to understand the processes that drive the observed gradual moistening of the troposphere prior to the triggering of an MJO event (Yoneyama et al. 2013). Using high-frequency atmospheric moisture measurements (HSRL and soundings) with cloud observations (C-band radar and ceilometer) on board R/V *Mirai*, we have been able to show the rapid variations of moisture associated with shallow convection on various scales. Specifically, we provide the first estimate of local and instantaneous (a few kilometers and a few tens of minutes, respectively) moisture anomalies and tendencies linked with shallow convective clouds. Moisture anomalies of approximately 0.2–$0.5\,\mathrm{g\,kg^{-1}}$ and moistening on the order of 10–$20\,\mathrm{g\,kg^{-1}\,day^{-1}}$ at 1–4-km heights and drying on the order of $-10\,\mathrm{g\,kg^{-1}\,day^{-1}}$ below the cloud bases are reported. Our analysis also shows that these shallow convective clouds have a typical horizontal extent of 0.5–1 km associated with moisture anomalies with horizontal scales of a few kilometers. We then reveal the moisture tendencies associated with shallow convective clouds on the mesoscale (tens to hundreds of kilometers) using both HSRL and sounding data. Moisture anomalies on the order of 0.5–$1\,\mathrm{g\,kg^{-1}}$ are linked with local maxima of shallow convection and persist for a few hours. This finding is consistent with the analysis of Powell and Houze (2013) using AMIE observations on Addu Atoll during the same period. The associated tendencies, which are obtained using two independent datasets, have comparable orders of magnitude and correspond to a moistening of the lower free troposphere of approximately 1–$4\,\mathrm{g\,kg^{-1}\,day^{-1}}$ between 1- and 4-km heights. Yet an intriguing feature is that the HSRL data suggest moisture anomalies from 1- to 4-km heights, whereas the soundings data suggest that moisture anomalies are usually strong at 2 km and below. This discrepancy may arise because of the relatively low temporal resolution of the soundings data preventing them from capturing the moistening by shallow clouds between 2 and 4 km.

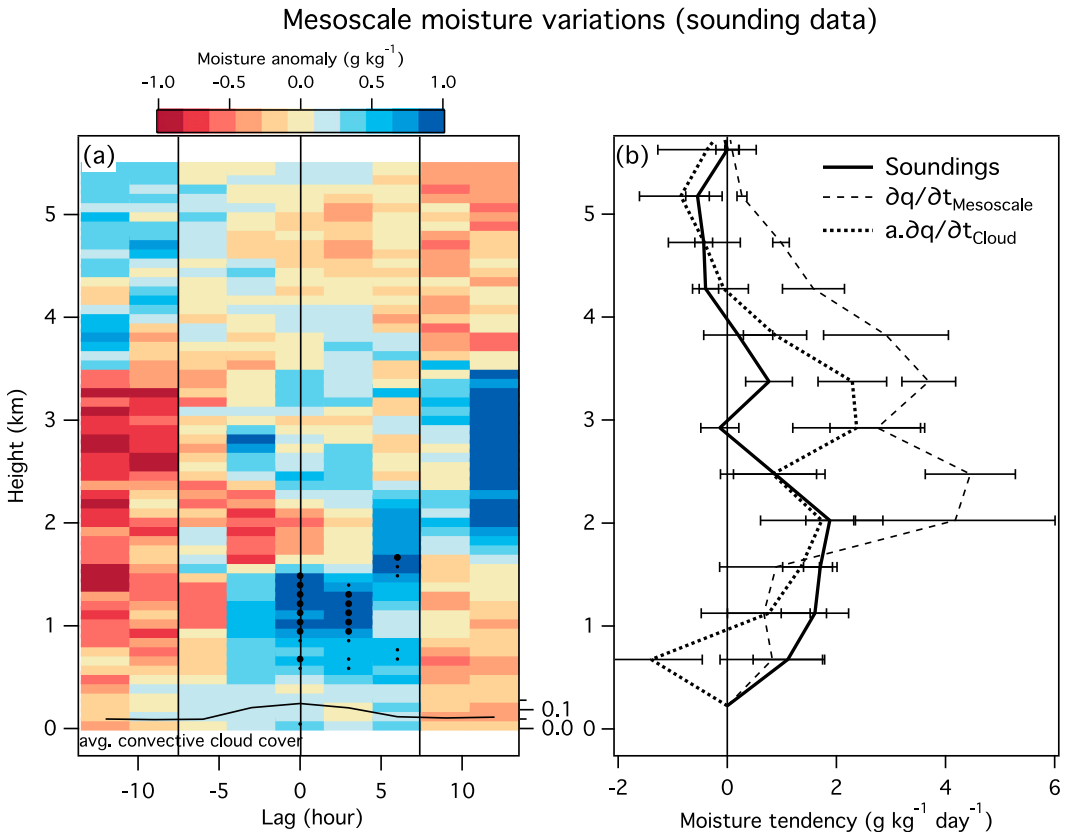

FIG. 9. (a) As in Fig. 4a, the composite of the sounding moisture anomalies is constructed relative to the maxima (>5%) in the 3-h convective cloud cover for shallow convection situations (34 cases); the number of degrees of freedom is 10–34. Note that only maxima that occur during nighttime are considered here. (b) As in Fig. 4b, the mean moisture tendency profile (soundings, solid thick) is computed from (a) at ±7.5 h [vertical lines on (a)] following the same approach, but using HSRL data ($\partial q/\partial t_{\text{Mesoscale}}$; dashed) and following Eq. (3) with the mean convective cloud cover at lag 0 ($a\partial q/\partial t_{\text{Cloud}}$; dotted line; a = 15%).

Yet this is where the moisture is likely to impact the shallow-to-deep-convection transition (e.g., Jensen and Del Genio 2006). Thus, caution should be taken when using low-temporal-resolution (3 h or above) data to estimate moistening by mesoscale convective cloud activities. The mesoscale low-tropospheric moistening associated with shallow convection is consistent with the observed mean convective cloud coverage at lag 0 following Eq. (3). The orders of magnitude of our estimates of moisture variations at different temporal and spatial scales are thus consistent with one another and with the assumption that they are mainly the result of convection.

The observations presented here are preliminary, and further work is necessary to better quantify the impact of shallow convection on the low-level moisture in all types of conditions. The local moisture tendencies presented in this study are the result of 1) the advection and spread of the convective cloud humidity halo by the wind and 2) the change in moisture due to detrainment of active clouds or evaporation of decaying clouds. These processes certainly depend on the cloud's environment: that is, the wind profile that influences the cloud advection and propagation (Telford and Wagner 1980) and the thermodynamic structure of the boundary layer that influences the layer at which clouds detrain (Perry and Hobbs 1996; Davison et al. 2013). Another interesting question is whether nonprecipitating clouds are more effective in moistening the troposphere than precipitating clouds, as suggested by Rapp et al. (2011). The moisture tendencies associated with shallow convection may change during the cloud's life cycle. Thus, any factor controlling the life cycle of shallow convection (i.e., the relative duration of the mature stage over the decaying stage) should also impact the moisture tendencies associated with an ensemble of clouds. The increase in daytime sea surface temperature may, for instance, lead to enhanced shallow convection in the afternoon (Bellenger et al. 2010; Ruppert and Johnson 2015). Ruppert and Johnson (2015) showed a significant daytime low-level moistening at Gan during a suppressed phase of the MJO during CINDY/DYNAMO.

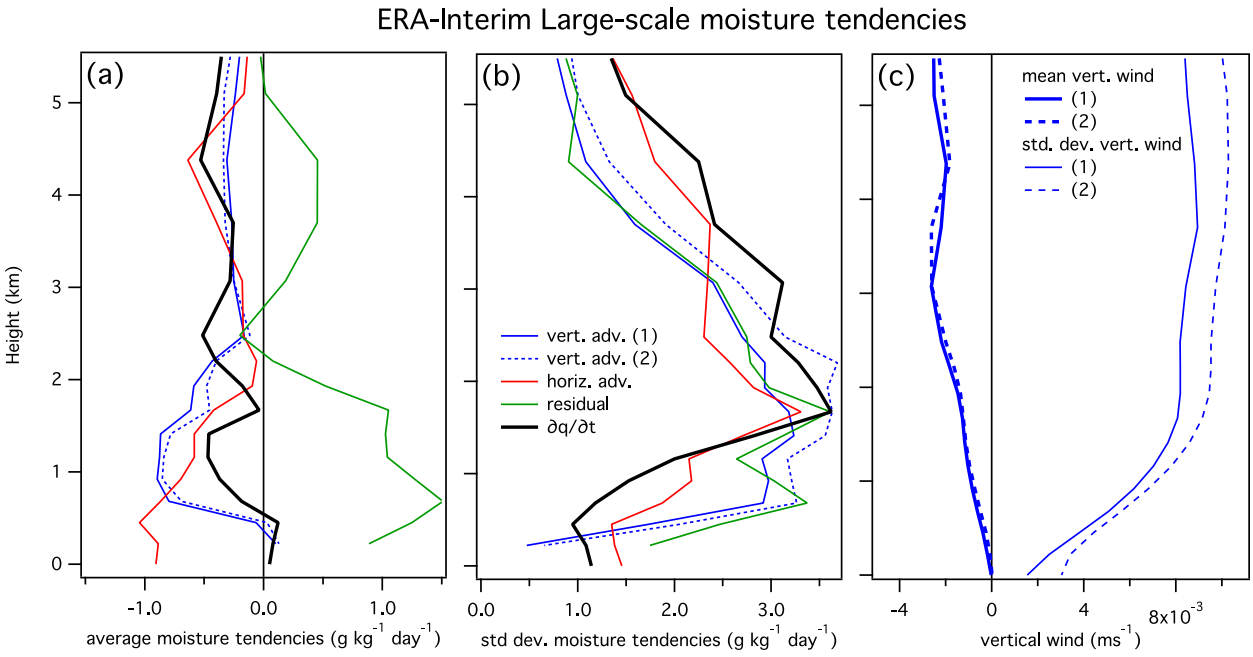

FIG. 10. Large-scale moisture budget from ERA-Interim over a 200 km × 200 km region centered on the R/V *Mirai* position for shallow convective situations during nighttime (43 cases): (a) mean and (b) standard deviation profiles for local moisture tendency (thick black) and its different components [vertical moisture advection (blue), horizontal moisture (red), and evaporation/condensation and subgrid processes computed as a residual from Eq. (1) (green)], and (c) the mean vertical wind speed (thick) and its standard deviation (thin). The dashed blue lines represent the vertical advection in (a) and (b) and the vertical wind in (c) computed using Eq. (2).

This could be due to either more numerous shallow cumulus clouds (greater convective cloud cover) or more active convective clouds (greater $\partial q/\partial t_{\text{Cloud}}$). Our diagnostic based on nighttime HSRL data may then underestimate the average moisture variations associated with shallow convection. Furthermore, we can only accurately monitor moisture variations below 4 km, whereas moistening by congestus at 5–6-km heights is arguably important.

Despite these uncertainties, the mesoscale moisture tendencies presented here are consistent with previous results using bulk computations, LESs (Hohenegger and Stevens 2013; Waite and Khouider 2010), and in situ estimates from a network of soundings (e.g., Schumacher et al. 2008; Katsumata et al. 2013). Schumacher et al. (2008) found an apparent moistening of approximately $1\,\text{g kg}^{-1}\,\text{day}^{-1}$ at approximately 2 km associated with shallow cumulus clouds during the Kwajalein Experiment (KWAJEX). During the preactive phase of an intraseasonal event, Katsumata et al. (2013) found moisture sources of approximately $0.8\,\text{g kg}^{-1}\,\text{day}^{-1}$ at approximately 2–3 km on average that could reach up to $2.5\,\text{g kg}^{-1}\,\text{day}^{-1}$. So, at the scale of a usual atmospheric global circulation model, the average moisture tendency associated with shallow convection has a robust order of magnitude. These results should be helpful to validate and develop parameterizations of moisture transport by shallow convection in these models.

The role of shallow convection and congestus in moistening the lower troposphere and preconditioning the atmosphere for an MJO trigger has been recently questioned (Hohenegger and Stevens 2013; Kumar et al. 2013). By studying convective events at Darwin, Kumar et al. (2013) showed a $1–2\,\text{g kg}^{-1}\,\text{day}^{-1}$ moistening due to subgrid-scale processes below 5 km that occurred 5–12 h prior to the rainfall maximum (see their Fig. 12a). They attribute this moistening to the evaporation of stratiform rainfall and argue that no congestus clouds were observed at that time. However, the moisture tendency is comparable to our finding and could also be the result of shallow convection, which can be underestimated by the C-band radar that they used (e.g., Feng et al. 2014). According to Hohenegger and Stevens (2013), moistening by shallow convection on the order of $1–2\,\text{g kg}^{-1}\,\text{day}^{-1}$ is not sufficient to explain the usually observed rapid transition from shallow to deep convection. Synoptic-scale dynamical perturbations, such as equatorial Kelvin waves, Rossby waves, mixed Rossby–gravity waves, and vortices associated with tropical depressions are indeed active in the Indian Ocean during CINDY/DYNAMO (Gottschalck et al. 2013; Kerns and Chen 2014). These perturbations strongly impact the

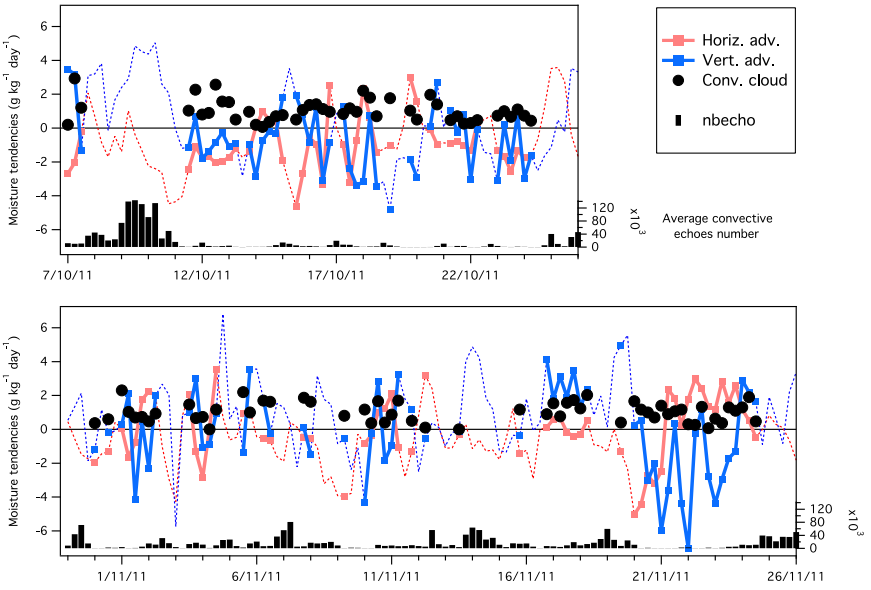

FIG. 11. Time series (g kg^{-1} day^{-1}) of ERA-Interim horizontal (red) and vertical (blue) advection terms averaged between 1- and 4-km heights and the moisture input by shallow clouds (black circles) computed following Eq. (3) with the mean $\partial q/\partial t_{\text{Cloud}}$ between 1 and 4 km and the ceilometer-derived convective cloud coverage for 6-h time steps. The moistening by shallow convection is only evaluated for shallow convection situations. The total number of convective echoes observed by the C-band radar is also reported (black bars; right vertical axis). Large-scale tendencies for shallow convective situations are plotted as solid lines with square markers, and all other situations are depicted as thin dashed lines.

moisture fields. Large-scale advection tendencies (horizontal and vertical) at the R/V *Mirai* position show very strong temporal variability and can be several times larger than the mean moisture tendency associated with shallow convection (see Fig. 11). For instance, there is the strong positive vertical moisture advection during 9–10 October associated with deep convection or the dry-air surge around 20 November described by Kerns and Chen (2014) that caused strong negative horizontal moisture advection at the R/V *Mirai* position. Furthermore, local tropospheric moisture is certainly not the only important factor that can explain the triggering of an MJO. Kerns and Chen (2014) suggested, for instance, that the subsidence over equatorial regions that prevents the triggering of deep convection could be diminished by the suppression of the convection in the ITCZ by dry-air surges. Then horizontal advection (of dry air here) may have a nonlocal impact on the transition from shallow to deep convection over the equator and on the MJO triggering.

Yet the moistening associated with shallow convection can be one of the leading terms in the large-scale moisture budget over a few days in shallow cumulus regimes (e.g., 16–17 October 2011, Fig. 11). In addition, because all types of convection are present during any given MJO phase (e.g., Riley et al. 2011; Zuluaga and Houze 2013; Powell and Houze 2013; Barnes and Houze 2013; Xu and Rutledge 2014), shallow convection may be a constant moisture supply for the lower troposphere; by contrast, large-scale advective tendencies can cancel out their effect on the scale of a few days. Thus, the relative role played by shallow convection as a steady source in the moisture budget can change depending on the considered time scale. In addition to this local effect, shallow convection may also have a remote effect through large-scale advection. Figure 10a indeed suggests that part of the humidification by shallow convection is transported away by horizontal advection. At the R/V *Mirai* position, shallow convection largely prevailed during the SOP upwind of the MJO activity that was observed farther north (Yoneyama et al. 2013; Johnson and Ciesielski 2013). These effects have yet to be quantified to fully understand the role played by shallow convection in phenomena such as the MJO. Recent studies indeed suggested that shallow convection may be necessary to properly simulate the MJO and its eastward propagation (e.g., Zhang and Song 2009; Cai et al. 2013).

Note that these conclusions are drawn from observations of the ITCZ where a weak MJO signal was observed. Therefore, one should be cautious when extending the present conclusions to the MJO. In addition, the MJO shows a great interevent variability that may partly

depend on the large-scale circulation (e.g., Bellenger and Duvel 2012; Duvel et al. 2013). Johnson and Ciesielski (2013) showed that preconditioning exhibited different time scales for the first two CINDY/DYNAMO MJO events that were observed during the SOP. This suggests that the relative importance of the different processes involved in the moisture buildup may strongly vary from one event to another. Detailed case studies of different events should be performed to understand the variability behind the average picture presented by Benedict and Randall (2007). For instance, the shallow conditional instability of the second kind (CISK) hypothesized by Wu (2003), which would result in response to spatially organized shallow convection and congestus clouds, might have an impact on the preconditioning time scale. The efficiency of convection in moistening the troposphere may further depend on large-scale environmental factors, such as the sea surface temperature or the relative humidity, as already discussed. Such sensitivity is, however, not explored here. In addition to MJO, we still have to determine the role of convection moistening in phenomena for which the coupling between dynamics and thermodynamics plays a central role (e.g., the convectively coupled Kelvin waves) or in the recovery of lower-tropospheric moisture after a dry intrusion (e.g., Redelsperger et al. 2002).

Finally, the use of high-frequency moisture data from HSRL on board R/V *Mirai* proved useful in monitoring rapid moisture variations in the lowest few kilometers of the atmosphere. However, it may be difficult to use ground-based lidar to depict moisture variations above 4 km where moistening associated with deeper congestus may be important. In addition, it was not possible to sort the clouds observed at the vessel location by their actual vertical extension to precisely determine their detrainment profiles. To do so, the use of vertically pointing cloud radar would certainly be of great interest. However, because of technical issues, the data from CINDY/DYNAMO are not yet available. Additional observations are certainly necessary to gain confidence in the evaluation of convection-related moisture variations and to explore their sensitivity to the environment in which it occurs. Such results would provide better insight into the physics of complex phenomena that involve convection, such as MJO or equatorial convectively coupled waves, and would reduce climate projection uncertainties. The results would also provide useful constraints for the validation of large-eddy simulations, cloud-resolving models, and convective parameterizations.

Acknowledgments. The authors express their thanks to Captain Y. Ishioka and his crew and technical staff of Global Ocean Development, Inc. for their support of observations onboard R/V *Mirai*. The authors also thank the editor, the three anonymous reviewers, and Dr. Fabio D'Andrea for their constructive comments and suggestions, which helped improve this article. CINDY/DYNAMO/AMIE/LASP were sponsored by NSF, NOAA, DOE, ONR, NASA, and JAMSTEC.

REFERENCES

Agudelo, P. A., J. A. Curry, C. D. Hoyos, and P. J. Webster, 2006: Transition between suppressed and active phases of intraseasonal oscillations in the Indo-Pacific warm pool. *J. Climate,* **19,** 5519–5530, doi:10.1175/JCLI3924.1.

Barnes, H. C., and R. A. Houze Jr., 2013: The precipitating cloud population of the Madden–Julian Oscillation over the Indian and west Pacific Oceans. *J. Geophys. Res. Atmos.,* **118,** 6996–7023, doi:10.1002/jgrd.50375.

Bellenger, H., and J. P. Duvel, 2012: The event-to-event variability of the boreal winter MJO. *Geophys. Res. Lett.,* **39,** L08701, doi:10.1029/2012GL051294.

——, Y. N. Takayabu, T. Ushiyama, and K. Yoneyama, 2010: Role of diurnal warm layers in the diurnal cycle of convection over the tropical Indian Ocean during MISMO. *Mon. Wea. Rev.,* **138,** 2426–2433, doi:10.1175/2010MWR3249.1.

Benedict, J. J., and D. A. Randall, 2007: Observed characteristics of the MJO relative to maximum rainfall. *J. Atmos. Sci.,* **64,** 2332–2354, doi:10.1175/JAS3968.1.

Cai, Q., G. J. Zhang, and T. Zhou, 2013: Impact of shallow convection on MJO simulation: A moist static energy and moisture budget analysis. *J. Climate,* **26,** 2417–2431, doi:10.1175/JCLI-D-12-00127.1.

Ciesielski, P. E., and Coauthors, 2014: Quality-controlled upper-air sounding dataset for DYNAMO/CINDY/AMIE: Development and corrections. *J. Atmos. Oceanic Technol.,* **31,** 741–764, doi:10.1175/JTECH-D-13-00165.1.

Davison, J. L., R. M. Rauber, L. Di Girolamo, and M. A. LeMone, 2013: A revised conceptual model of the tropical marine boundary layer. Part III: Bragg scattering layer statistical properties. *J. Atmos. Sci.,* **70,** 3047–3062, doi:10.1175/JAS-D-12-0323.1.

Dee, D. P., and Coauthors, 2011: The ERA-Interim reanalysis: Configuration and performance of the data assimilation system. *Quart. J. Roy. Meteor. Soc.,* **137,** 553–597, doi:10.1002/qj.828.

Del Genio, A. D., Y. Chen, D. Kim, and M.-S. Yao, 2012: The MJO transition from shallow to deep convection in *CloudSat*/CALIPSO data and GISS GCM simulations. *J. Climate,* **25,** 3755–3770, doi:10.1175/JCLI-D-11-00384.1.

Duvel, J. P., H. Bellenger, G. Bellon, and M. Remaud, 2013: An event-by-event assessment of tropical intraseasonal perturbations for general circulation models. *Climate Dyn.,* **40,** 857–873, doi:10.1007/s00382-012-1303-6.

Feng, Z., S. A. McFarlane, C. Schumacher, S. Ellis, J. Comstock, and N. Bharadwaj, 2014: Constructing a merged cloud–precipitation radar dataset for tropical convective clouds during the DYNAMO/AMIE experiment at Addu Atoll. *J. Atmos. Oceanic Technol.,* **31,** 1021–1042, doi:10.1175/JTECH-D-13-00132.1.

Gottschalck, J., P. E. Roundy, C. J. Schreck III, A. Vintzileos, and C. Zhang, 2013: Large-scale atmospheric and oceanic conditions during the 2011–12 DYNAMO field campaign. *Mon. Wea. Rev.,* **141,** 4173–4196, doi:10.1175/MWR-D-13-00022.1.

Hohenegger, C., and B. Stevens, 2013: Preconditioning deep convection with cumulus congestus. *J. Atmos. Sci.,* **70,** 448–464, doi:10.1175/JAS-D-12-089.1.

Holloway, C. E., and J. D. Neelin, 2009: Moisture vertical structure, column water vapor, and tropical deep convection. *J. Atmos. Sci.,* **66,** 1665–1683, doi:10.1175/2008JAS2806.1.

Jensen, M. P., and A. D. Del Genio, 2006: Factors limiting convective cloud-top height at the ARM Nauru Island climate facility. *J. Climate,* **19,** 2105–2117, doi:10.1175/JCLI3722.1.

Johnson, R. H., and P. E. Ciesielski, 2013: Structure and properties of Madden–Julian oscillations deduced from DYNAMO sounding arrays. *J. Atmos. Sci.,* **70,** 3157–3179, doi:10.1175/JAS-D-13-065.1.

——, T. M. Rickenbach, S. A. Rutledge, P. E. Ciesielski, and W. H. Schubert, 1999: Trimodal characteristics of tropical convection. *J. Climate,* **12,** 2397–2418, doi:10.1175/1520-0442(1999)012<2397:TCOTC>2.0.CO;2.

——, P. E. Ciesielski, and J. A. Cotturone, 2001: Multiscale variability of the atmospheric mixed layer over the western Pacific warm pool. *J. Atmos. Sci.,* **58,** 2729–2749, doi:10.1175/1520-0469(2001)058<2729:MVOTAM>2.0.CO;2.

Katsumata, M., T. Ushiyama, K. Yoneyama, and Y. Fujiyoshi, 2008: Combined use of TRMM/PR and disdrometer data to correct reflectivity of ground-based radars. *SOLA,* **4,** 101–104, doi:10.2151/sola.2008-026.

——, H. Yamada, H. Kubota, Q. Moteki, and R. Shirooka, 2013: Observed evolution of northward-propagating intraseasonal variation over the western Pacific: A case study in boreal early summer. *Mon. Wea. Rev.,* **141,** 690–706, doi:10.1175/MWR-D-12-00011.1.

Kemball-Cook, S., and B. C. Weare, 2001: The onset of convection in the Madden–Julian oscillation. *J. Climate,* **14,** 780–793, doi:10.1175/1520-0442(2001)014<0780:TOOCIT>2.0.CO;2.

Kerns, B. W., and S. S. Chen, 2014: Equatorial dry air intrusion and related synoptic variability in MJO initiation during DYNAMO. *Mon. Wea. Rev.,* **142,** 1326–1343, doi:10.1175/MWR-D-13-00159.1.

Kikuchi, K., and Y. N. Takayabu, 2004: The development of organized convection associated with the MJO during TOGA COARE IOP: Trimodal characteristics. *Geophys. Res. Lett.,* **31,** L10101, doi:10.1029/2004GL019601.

Kuang, Z., and C. S. Bretherton, 2006: A mass-flux scheme view of a high-resolution simulation of a transition from shallow to deep cumulus convection. *J. Atmos. Sci.,* **63,** 1895–1909, doi:10.1175/JAS3723.1.

Kumar, V. V., C. Jakob, A. Protat, P. T. May, and L. Davies, 2013: The four cumulus cloud modes and their progression during rainfall events: A C-band polarimetric radar perspective. *J. Geophys. Res. Atmos.,* **118,** 8375–8389, doi:10.1002/jgrd.50640.

Laird, N. F., 2005: Humidity halo surrounding small cumulus clouds in a tropical environment. *J. Atmos. Sci.,* **62,** 3420–3425, doi:10.1175/JAS3538.1.

Mapes, B. E., S. Tulich, J. Lin, and P. Zuidema, 2006: The mesoscale convection life cycle: Building block or prototype for large-scale tropical waves? *Dyn. Atmos. Oceans,* **42,** 3–29, doi:10.1016/j.dynatmoce.2006.03.003.

Masunaga, H., 2013: A satellite study of tropical moist convection and environmental variability: A moisture and thermal budget analysis. *J. Atmos. Sci.,* **70,** 2443–2464, doi:10.1175/JAS-D-12-0273.1.

Nasuno, T., 2013: Forecast skill of Madden–Julian Oscillation events in a global nonhydrostatic model during the CINDY2011/DYNAMO observation period. *SOLA,* **9,** 69–73, doi:10.2151/sola.2013-016.

Nishizawa, T., N. Sugimoto, I. Matsui, and T. Takano, 2012: Development of two-wavelength high-spectral-resolution lidar and application to shipborne measurements. *Proc. 26th Int. Laser Radar Conf.,* Porto Heli, Greece, 147–150.

Nitta, T., and S. Esbensen, 1974: Heat and moisture budget analyses using BOMEX data. *Mon. Wea. Rev.,* **102,** 17–28, doi:10.1175/1520-0493(1974)102<0017:HAMBAU>2.0.CO;2.

Perry, K. D., and P. V. Hobbs, 1996: Influences of isolated cumulus clouds on the humidity of their surroundings. *J. Atmos. Sci.,* **53,** 159–174, doi:10.1175/1520-0469(1996)053<0159:IOICCO>2.0.CO;2.

Powell, S. W., and R. A. Houze Jr., 2013: The cloud population and onset of the Madden–Julian Oscillation over the Indian Ocean during DYNAMO-AMIE. *J. Geophys. Res. Atmos.,* **118,** 11 979–11 995, doi:10.1002/2013JD020421.

Rapp, A. D., C. D. Kummerow, and L. Fowler, 2011: Interactions between warm rain clouds and atmospheric preconditioning for deep convection in the tropics. *J. Geophys. Res.,* **116,** D23210, doi:10.1029/2011JD016143.

Redelsperger, J.-L., D. B. Parsons, and F. Guichard, 2002: Recovery processes and factors limiting cloud-top height following the arrival of a dry intrusion observed during TOGA COARE. *J. Atmos. Sci.,* **9,** 2438–2457, doi:10.1175/1520-0469(2002)059<2438:RPAFLC>2.0.CO;2.

Riley, E. M., B. E. Mapes, and S. N. Tulich, 2011: Clouds associated with the Madden–Julian oscillation: A new perspective from *CloudSat*. *J. Atmos. Sci.,* **68,** 3032–3051, doi:10.1175/JAS-D-11-030.1.

Rowe, A. K., and R. A. Houze Jr., 2014: Microphysical characteristics of MJO convection over the Indian Ocean during DYNAMO. *J. Geophys. Res. Atmos.,* **119,** 2543–2554, doi:10.1002/2013JD020799.

Ruppert, J. H., and R. H. Johnson, 2015: Diurnally modulated cumulus moistening in the preonset stage of the Madden–Julian oscillation during DYNAMO. *J. Atmos. Sci.,* doi:10.1175/JAS-D-14-0218.1, in press.

Sakai, T., T. Nagai, M. Nakazato, Y. Mano, and T. Matsumura, 2003: Ice clouds and Asian dust studied with lidar measurements of particle extinction-to-backscatter ratio, particle depolarization, and water-vapor mixing ratio over Tsukuba. *Appl. Opt.,* **42,** 7103–7116, doi:10.1364/AO.42.007103.

——, ——, ——, T. Matsumura, N. Orikasa, and Y. Shoji, 2007: Comparisons of Raman lidar measurements of tropospheric water vapor profiles with radiosondes, hygrometers on the meteorological observation tower, and GPS at Tsukuba, Japan. *J. Atmos. Oceanic. Technol.,* **24,** 1407–1423, doi:10.1175/JTECH2056.1.

Schumacher, C., P. E. Ciesielski, and M. H. Zhang, 2008: Tropical cloud heating profiles: Analysis from KWAJEX. *Mon. Wea. Rev.,* **136,** 4289–4300, doi:10.1175/2008MWR2275.1.

Steiner, M., R. A. Houze, and S. E. Yuter, 1995: Climatological characterization of three-dimensional storm structure from operational radar and rain gauge data. *J. Appl. Meteor.,* **34,** 1978–2007, doi:10.1175/1520-0450(1995)034<1978:CCOTDS>2.0.CO;2.

Straub, K. H., and G. N. Kiladis, 2002: Observations of a convectively coupled Kelvin wave in the eastern Pacific ITCZ. *J. Atmos. Sci.,* **59,** 30–53, doi:10.1175/1520-0469(2002)059<0030:OOACCK>2.0.CO;2.

Takayabu, Y. N., K.-M. Lau, and C.-H. Sui, 1996: Observation of a quasi-2-day wave during TOGA COARE. *Mon. Wea. Rev.,* **124,** 1892–1913, doi:10.1175/1520-0493(1996)124<1892:OOAQDW>2.0.CO;2.

——, J. Yokomori, and K. Yoneyama, 2006: A diagnostic study on interactions between atmospheric thermodynamic structure and cumulus convection over the tropical western Pacific

Ocean and over the Indochina Peninsula. *J. Meteor. Soc. Japan,* **84A,** 151–169, doi:10.2151/jmsj.84A.151.

Telford J. W., and P. B. Wagner, 1980: The dynamical and liquid water structure of the small cumulus as determined from its environment. *Pure Appl. Geophys.,* **118,** 935–952, doi:10.1007/BF01593041.

Thayer-Calder, K., and D. A. Randall, 2009: The role of convective moistening in the Madden–Julian oscillation. *J. Atmos. Sci.,* **66,** 3297–3312, doi:10.1175/2009JAS3081.1.

Trenberth, K. E., 1991: Climate diagnostics from global analyses: Conservation of mass in ECMWF analyses. *J. Climate,* **4,** 707–722, doi:10.1175/1520-0442(1991)004<0707:CDFGAC>2.0.CO;2.

Waite, M. L., and B. Khouider, 2010: The deepening of tropical convection by congestus preconditioning. *J. Atmos. Sci.,* **67,** 2601–2615, doi:10.1175/2010JAS3357.1.

Wu, Z., 2003: A shallow CISK, deep equilibrium mechanism for the interaction between large-scale convection and large-scale circulations in the tropics. *J. Atmos. Sci.,* **60,** 377–392, doi:10.1175/1520-0469(2003)060<0377:ASCDEM>2.0.CO;2.

Xu, W., and S. Rutledge, 2014: Convective characteristics of the Madden–Julian Oscillation over the central Indian Ocean observed by shipborne radar during DYNAMO. *J. Atmos. Sci.,* **71,** 2859–2877, doi:10.1175/JAS-D-13-0372.1.

Yanai, M., S. Esbensen, and J.-H. Chu, 1973: Determination of bulk properties of tropical cloud clusters from large-scale heat and moisture budgets. *J. Atmos. Sci.,* **30,** 611–627, doi:10.1175/1520-0469(1973)030<0611:DOBPOT>2.0.CO;2.

Yoneyama, K., C. Zhang, and C. N. Long, 2013: Tracking pulses of the Madden–Julian oscillation. *Bull. Amer. Meteor. Soc.,* **94,** 1871–1891, doi:10.1175/BAMS-D-12-00157.1.

Yuter, S. E., R. A. Houze Jr., E. A. Smith, T. T. Wilheit, and E. Zipser, 2005: Physical characterization of tropical oceanic convection observed in KWAJEX. *J. Appl. Meteor.,* **44,** 385–415, doi:10.1175/JAM2206.1.

Zelinka, M. D., and D. L. Hartmann, 2009: Response of humidity and clouds to tropical deep convection. *J. Climate,* **22,** 2389–2404, doi:10.1175/2008JCLI2452.1.

Zhang, C., 2005: Madden–Julian Oscillation. *Rev. Geophys.,* **43,** RG2003, doi:10.1029/2004RG000158.

Zhang, G. J., and X. Song, 2009: Interaction of deep and shallow convection is key to Madden–Julian Oscillation simulation. *Geophys. Res. Lett.,* **36,** L09708, doi:10.1029/2009GL037340.

Zuidema, P., 1998: The 600–800-mb minimum in tropical cloudiness observed during TOGA COARE. *J. Atmos. Sci.,* **55,** 2220–2228, doi:10.1175/1520-0469(1998)055<2220:TMMITC>2.0.CO;2.

——, and Coauthors, 2012: On trade wind cumulus cold pools. *J. Atmos. Sci.,* **69,** 258–280, doi:10.1175/JAS-D-11-0143.1.

Zuluaga, M. D., and R. A. Houze, 2013: Evolution of the population of precipitating convective systems over the equatorial Indian Ocean in active phases of the Madden–Julian oscillation. *J. Atmos. Sci.,* **70,** 2713–2725, doi:10.1175/JAS-D-12-0311.1.